Applied Radiation and Isotopes 181 (2022) 110093

Contents lists available at ScienceDirect

Applied Radiation and Isotopes

journal homepage: www.elsevier.com/locate/apradiso

Ion implantation of ^{226}Ra for a primary ^{222}Rn emanation standard

Florian Mertes [a,*], Nina Kneip [b], Reinhard Heinke [b], Tom Kieck [b], Dominik Studer [b], Felix Weber [b], Stefan Röttger [a], Annette Röttger [a], Klaus Wendt [b], Clemens Walther [c]

[a] Physikalisch-Technische Bundesanstalt, Bundesallee 100, 38116, Braunschweig, Germany
[b] Johannes Gutenberg-Universität Mainz, Institut für Physik, Staudingerweg 7, 55128, Mainz, Germany
[c] Leibniz Universität Hannover, Institut für Radioökologie und Strahlenschutz, 30419, Hannover, Germany

ARTICLE INFO

Keywords:
Ion implantation
^{222}Rn emanation
Laser ionization
Defined solid-angle alpha-particle spectrometry

ABSTRACT

Laser resonance ionization at the RISIKO 30 kV mass separator has been used to produce isotopically and isobarically pure and well quantified ^{222}Rn emanation standards. Based upon laser-spectroscopic preparation studies, ion implantation into aluminum and tungsten targets has been carried out, providing overall implantation efficiencies of 40% up to 60%. The absolute implanted activity of ^{226}Ra was determined by the technique of defined solid-angle α-particle spectrometry, where excellent energy resolution was observed. The ^{222}Rn emanation coefficient of the produced targets was studied using α-particle and γ-ray spectrometry, and yielded results between 0.23 and 0.34, with relative uncertainty on the order of 1%. No dependence exceeding a 1% change of the emanation on humidity could be identified in the range of 15 %rH to 75 %rH, whereas there were hints of a slight correlation between the emanation and temperature. Additionally, and as expected, the emanation coefficient was found to be dependent on the target material as well as the implanted dose.

1. Introduction

National and international guidelines and regulations drive the need for SI-traceable measurements of ^{222}Rn at very low activity concentrations (<300 Bq·m^{-3}) in air. For such low concentrations, conventional gaseous standards of ^{222}Rn are not suitable for the calibration of measurement devices because the decaying nature of reference atmospheres produced in this way results in poor counting statistics. An alternative was found relatively recently in ^{222}Rn emanation standards (Linzmaier and Röttger, 2013; Mertes et al., 2020), which are ^{226}Ra sources constructed in such a way that a known amount of ^{222}Rn is released from them per unit time. Emanation standards can thus be used to produce time-stable reference atmospheres with the potential to overcome the poor counting statistics from decaying atmospheres. However, the processes leading to the release of ^{222}Rn are usually diffusion processes, such that they correlate with the climate parameters of the environment the sources are operated in. In this work, we investigated the use of ion implantation of ^{226}Ra for the construction of ^{222}Rn emanation sources.

To ionize ^{226}Ra for this purpose, resonance ionization mass spectrometry (RIMS), which is a highly efficient tool to produce ultra-pure mono-isotopic ion beams for various applications including the collection or implantation of ultra-pure isotopic samples, is used. The technique is commonly applied at on-line radioactive ion beam facilities such as CERN-ISOLDE (Fedosseev et al., 2017) or TRIUMF-ISAC (Lassen et al., 2017) for efficient production of exotic nuclides as well as off-line for rare isotope purification and enrichment. A suitable facility for the latter is the RISIKO mass separator at Mainz University used for ^{163}Ho purification for the ECHo neutrino mass experiment (Kieck et al., 2019b) and other similar tasks.

Resonant laser ionization involves efficient stepwise excitation of an atomic valence electron along strong optical transitions into the ionization continuum using high-power tunable pulsed laser sources. Due to the individual atomic structure of each chemical element, this process is highly selective in the suppression of initial isobaric contaminations. The combination with high transmission mass separation, e.g., in a magnetic sector field separator, adds suppression of isotopic contamination, resulting in a highly pure mono-isotopic ion beam. On the other hand, a careful choice of a suitable optical excitation ladder for each element of interest and application is of primary relevance and must be made considering the laser system at hand.

In the following, we discuss the case of RIMS on radium, specifically the isotope ^{226}Ra, in the context of the production of high quality, low-level ^{222}Rn emanation standards by ion implantation, intended for the generation of primary, time-stable, and SI-traceable ^{222}Rn reference

* Corresponding author.
E-mail address: florian.mertes@ptb.de (F. Mertes).

https://doi.org/10.1016/j.apradiso.2021.110093
Received 22 September 2021; Received in revised form 2 December 2021; Accepted 28 December 2021
Available online 31 December 2021

atmospheres below 300 Bq ·m^{-3}. For such sources, the ion implantation process should provide significant metrological benefits compared to the more traditional approaches of gravimetrical drop-casting of standardized solutions (Linzmaier and Röttger, 2013) or electrodeposition (Jurado Vargas and Fernández De Soto, 1996; Mertes et al., 2020). Specifically, enhanced stability concerning environmental changes and improvement in the accuracy of applied characterization techniques is expected and was checked systematically. For complete characterization of the sources, detailed measurements on the ^{222}Rn emanation coefficients, which describe the percentage of emitters that undergo exhalation, were carried out. For this purpose, the ratio of the residual ^{222}Rn and ^{226}Ra activities in the source was measured using γ-ray spectrometry of the progeny and α-particle spectrometry. Moreover, the approach of ion current measurements for implantation efficiency determination is compared with defined solid-angle α-particle spectrometry, allowing the determination of absolute ^{226}Ra activity.

1.1. Laser resonance ionization of radium

For the ionization of radium, the Mainz University Ti:sapphire (Ti:Sa) laser system is used (Mattolat et al., 2009; Rothe et al., 2011), which is pumped by a commercial frequency-doubled Nd:YAG laser (Photonics Industries DM100-532) at 532 nm, operating with a high pulse repetition rate of 10 kHz for efficient temporal overlap with a continuous evaporation source. An average output power in the range of 0.3 W–1.5 W in the blue to UV spectral range can be achieved by intra-cavity second harmonic generation (Sonnenschein et al., 2015) with a typical spectral linewidth of 7 GHz and a pulse length of 50 ns. The emission wavelength of the Ti:Sa laser used in this work, which is a modified development of the one presented in (Teigelhöfer et al., 2010), is selected by angle-tuning of a diffraction grating acting as end mirror of the resonator. This permits for rapid continuous wide range frequency tuning. Wavelengths are measured by a wavelength meter (High Finesse WSU-30).

In preparation for the radium implantation and extending earlier spectroscopic work (Wendt et al., 1987) and ionization scheme development (Day Goodacre et al., 2018; Raeder et al., 2014), different two-step ionization schemes were explored and compared at the RISIKO mass separator, which are presented in Fig. 1. The bottom panel shows the three tested two-step ionization schemes, for which the same first excitation step at 482.7 nm was used with ≈ 470 mW of laser light to populate the 20 715.7 cm^{-1} level along the strong $7s^2\ ^1S_0 \rightarrow 7s7p\ ^1P^o_1$ singlet transition (Kramida et al., 2020).

A long-range scan of the second excitation step in the range of the first ionization potential (IP) at 42 573.36 cm^{-1} and above is given in the top panel of Fig. 1. It shows a rather unstructured continuum without significant auto-ionizing states above the IP. The pronounced oscillatory structure between 43 100–43 450 cm^{-1} was caused by regular laser power fluctuations due to interference effects in the phase-matching process of the frequency doubling unit occurring during scans. Below the IP, series of Rydberg levels are clearly visible, which undergo efficient ionization by collisions, electric stray fields, black body radiation, or additional laser photons. A strong Rydberg level at 42 492.45 cm^{-1}, located about 80 cm^{-1} below the IP, was populated with 459.2 nm laser radiation and was tested for ionization, denominated as scheme A. Alternatively, non-resonant ionization was performed at two different wavelengths of 452.5 nm and 432.7 nm, denoted schemes B and C. A comparable signal intensity, representing the overall ionization efficiency, was achieved with scheme C with respect to scheme A and for simplicity, this scheme with non-resonant ionization was used for the radium implantations as no control and precise readjustment of the second step laser frequency is required. Note that within ion sources with strong electric fields the Rydberg ionization rate may be significantly enhanced.

1.2. Ion implantation of ^{226}Ra at RISIKO

The mass separator facility RISIKO combines a hot cavity laser ion source with magnetic sector field mass selection at a high voltage, high transmission device to produce isotopically and isobarically pure ion beams. To obtain ^{226}Ra samples for the ion implantation process, a ^{226}Ra solution of nominally 71 kBq ($RaCl_2$ with 0.5% m/m $BaCl_2{\cdot}2\ H_2O$ in 0.1 M HCl) was converted into the nitrate by addition and subsequent evaporation of concentrated HNO_3. It was purified from Ba^{2+} carriers by extraction chromatography through Sr-resin (Philip Horwitz et al., 2007) consisting of 4,4′ (5')-bis(tertbutylcyclohexano)-18-crown-6 in 1-butanol, dispersed on SiO_2-particles (TrisKem International), similar to the method reported in (Mertes et al., 2020). The Ba^{2+} extraction was monitored by gravimetrical addition of nominally 13 kBq $^{133}BaCl_2$ as a radiotracer for inactive Ba^{2+}, pooling those chromatography fractions in which no ^{133}Ba could be detected in the γ-ray spectrum. This sample preparation step was chosen to reduce space-charge effects from excessive amounts of Ba^{2+} and to avoid the excessive formation of $RaCl_2$ gas-phase molecules and $[RaCl]^+$ ions in the evaporator. During preparatory mass scans, the formation and ionization of $[RaCl]^+$ could still be observed from residual chloride contamination of the sample, stressing the need for this preparation step.

From the resultant solution of $^{226}Ra(NO_3)_2$ in 0.6 M HNO_3, desired

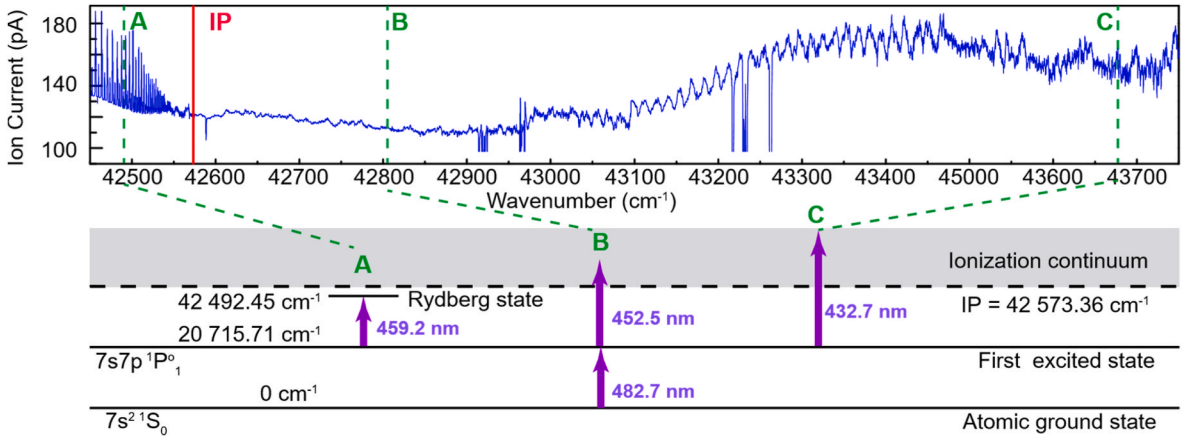

Fig. 1. Bottom: Two-step laser ionization schemes for radium ionization applied in this work. Electron configuration and level energies from (Kramida et al., 2020). Individual transitions A, B, and C are indicated at the corresponding energy positions of the spectrum above. **Top:** Long-range scan of the second excitation step from 42 450 cm^{-1} to 43 750 cm^{-1}. Signal dips between 42 900–43 000 cm^{-1} and 43 200–43 300 cm^{-1} occurred during ongoing laser and mass separator optimizations. For further details see text.

amounts of activity were drop-cast onto 5 × 5 mm^2 hafnium foils (97%, Goodfellow). The foils were folded afterward to fully enclose the sample and act as a reducing agent. The deposited ^{226}Ra activity on each foil was measured using γ-ray spectrometry with a high-purity germanium (HPGe) detector, comparing the 186 keV ^{226}Ra full-energy peak with a PTB reference ^{226}Ra point source.

For RIMS at the RISIKO facility, these ^{226}Ra samples were placed one at a time into a thin tantalum capillary (20 mm length, 1 mm inner diameter) acting as an independently heated sample reservoir. It is attached to the back of a tantalum tube furnace (34 mm length, 2.5 mm inner diameter) acting as an atomizer. A detailed schematic of the setup is given in (Kieck et al., 2019a). Both the sample reservoir and the atomizer are heated resistively. While the latter was kept at a constant temperature of about 2000 °C, as estimated from previous studies of the hot cavity setup (Kieck et al., 2019a), the sample reservoir was gradually heated slowly to allow controlled sample supply to the ion source. Ionization took place either unselectively by contact with the hot cavity walls (surface ionization), or specifically for the Ra atoms by laser resonance ionization. Due to the selectivity of the latter process, the relative contribution of unspecific background on the mass 226 was significantly reduced while in parallel the overall ionization efficiency was strongly increased in comparison to pure surface ionization. The ions were accelerated to a kinetic energy of 30 keV and shaped to form an ion beam by ion optical elements. Mass separation within the 60° dipole magnet achieved a resolving power of $m/\Delta m \approx 800$. After the separator slits at the focal plane of the magnet, the ion beam was post-focalized with an Einzel lens down to a beam size of 0.5 mm FWHM, permitting also for precise steering and spatial spot control for implantation into the different targets (Kieck et al., 2019b). The electrically conductive implantation targets were positioned one at a time within an insulated Faraday cup device (FC) including a repeller electrode put on −200 V potential for rejection of secondary electrons. This arrangement allows for permanent monitoring of the ion beam during implantation and reliable ion beam current quantification. A sketch of the overall experimental setup of the RISIKO mass separator with the laser system for resonance ionization is shown in Fig. 2.

Fig. 3 depicts the data from a typical implantation run with ion current plotted versus elapsed time. The curve progression can be separated into different *phases I, II,* and *III*. Controlled source heating enables reasonably steady evaporation and atomization of source atoms, as desirable for a proper resonance ionization process. During the initial *phase I* the goal of producing a radium ion beam with reasonably stable ion current was achieved and is visible in Fig. 3 by a small plateau at 1 pA. The low ion current during this phase was used to optimize the ion optics and the laser ionization process. These optimizations are very important to achieve high implantation efficiency. The main implantation *phase II*, specified by a relatively high ion beam current in the higher nA range, and correspondingly high implantation rate, has a typical duration in the range of 10 min–30 min depending on the ratio between ion current and activity of the sample. At RISIKO a maximum ion current in the range of a few 100 nA is known to ensure optimum transmission and implantation without ion beam degradation. Correspondingly, initial sample evaporation was controlled by careful heating of the sample reservoir, as the ^{226}Ra implantation was executed with a specifically low ion current of about 10 nA. Additionally, the atomizer cavity and reservoir were regularly baked out at the end of each measurement in *phase III* to purge the ion source from any remainders of the sample in preparation for the next implantation run. This also reduces influences of violent evaporation processes as observed at the end of the heating phase, for example. The ^{226}Ra ions produced during *phase III*

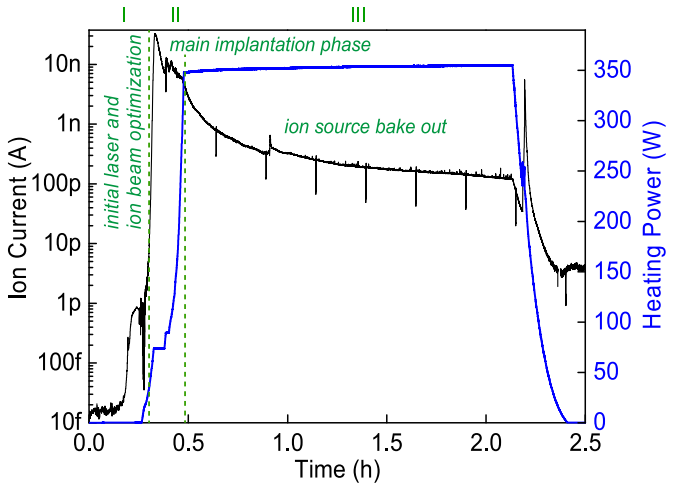

Fig. 3. Typical implantation process for the example of target 2018-1128. The black trace represents the ion current of implanted ^{226}Ra ions and the blue curve gives the heating power of the sample reservoir, which defines its temperature. The significant phases I, II, and III of the measurement are indicated, separated by the vertical dashed lines. (For interpretation of the references to color in this figure legend, the reader is referred to the Web version of this article.)

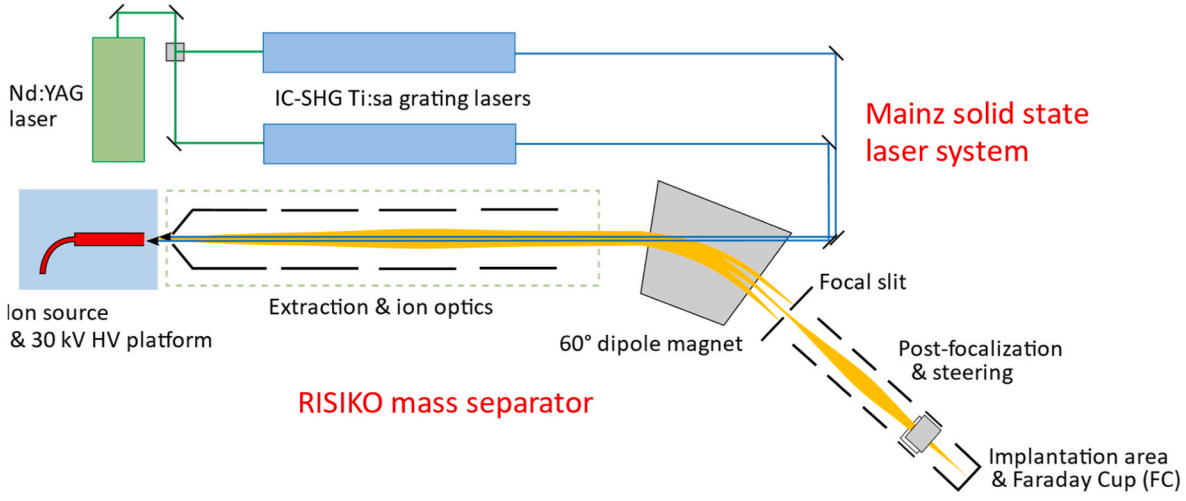

Fig. 2. Schematic sketch of the RISIKO laser mass separator facility for isotope separation and implantation. The ion beam is shown in yellow and the laser beams in blue. Details of the ion source and the implantation area including post-focalization and steering are discussed in the text. (For interpretation of the references to color in this figure legend, the reader is referred to the Web version of this article.)

were also implanted into the targets.

To quantify the targeted enhancement of laser resonance ionization over surface ionization, the lasers were blocked periodically with a shutter (signal dips in Fig. 3). Typically, an enhancement factor of significantly above 2 was demonstrated.

A total of 6 targets (3 tungsten sheets, 3 aluminum sheets) were implanted with ^{226}Ra with a total collection duration of about one to 2 h per target in a single implantation cycle. The collection duration varied corresponding to the desired implanted activity, the achieved ion current and the state of the sample in the ion source. The efficiency ε_C of the overall ^{226}Ra implantation process was defined as the ratio of activity A_C implanted into the target to the initial activity in the sample A_0 placed in the ion source, as previously determined by γ-ray spectrometry.

$$\varepsilon_C = \frac{A_C}{A_0} = \frac{\ln 2}{T_{1/2}} \frac{\int I \, \mathrm{d}t}{A_0 \, e} \tag{1}$$

A_C is extracted from the time-integrated ion current I for singly charged ions (total charge), measured on the target during implantation, while e is the elemental charge and $T_{1/2}$ is the half-life of ^{226}Ra, 1600 a (Bé et al., 2004). The ionization efficiency ε relates the number of atoms initially placed in the ion source to the number of atoms that are ultimately implanted into the target. It is composed of several factors, i.e., sample vaporization and atomization (avoiding molecule formation), the laser ionization process itself, ion survival in the atomizer cavity, extraction, ion beam formation, and transmission through the separator. Due to potential sputtering of already implanted material, the total collected charge given by the integrated ion current does not necessarily reflect the number of atoms that reside within the target after the implantation procedure.

Four samples, denoted S1, S2, S3, and S4, containing on the order of $N_0 \approx 10^{14}$ atoms of ^{226}Ra each (corresponding to the activities A_0) were used for the implantations into six circular targets of 30 mm nominal diameter and 1 mm thickness (obtained from Goodfellow, 99.5% W and 99.999% Al respectively). Each target was manually polished and cleaned with isopropyl alcohol before implantation. Results of the implantation process are compiled in Table 1. The A_α values represent the individual activities of implanted ^{226}Ra as determined by defined solid-angle α-particle spectrometry, as discussed in detail below. The implanted ion current, continuously recorded by the insulated Faraday cup implantation foil holder, delivered the implanted atom number which was used to derive A_C. Implantation efficiencies are calculated based on the radiometric results and the ion current integration, respectively, as indicated by the index α or C. As detailed in the *Discussion and Conclusions* section below, they are in overall good agreement.

Table 1
Overview of the implanted targets and initial sample sizes (activity per sample A_0) together with the implanted activity A_α and A_C, measured by α-particle spectrometry and ion current integration, respectively. In addition, efficiencies ε_C, derived from ion current integration as (A_C/A_0), and ε_α, derived from α-particle spectrometry as (A_α/A_0) are given. Uncertainties and systematic errors are discussed in the text.

Target (Material)	Sample A_0 (Bq)	A_α (Bq)	A_C (Bq)	A_C/A_α	ε_α (%)	ε_C (%)
2018-1120 (W)	S1 2500 (90)	922 (4)	766 (77)	0.83	36.9 (13)	30 (3)
2018-1121 (W)	S2 1940 (70)	1139 (5)	1155 (115)	1.01	58.7 (21)	60 (6)
2018-1122 (W)	S3 3080 (100)	671 (3)	724 (72)	1.07	35.4 (9)	32 (3)
2018-1128 (Al)		842 (4)	798 (80)	0.94		
2018-1133 (Al)	S4 3400 (90)	603 (3)	513 (51)	0.85	46.3 (15)	46 (5)
2018-1134 (Al)		514.2 (21)	475 (47)	0.92		

1.3. Defined solid angle α-particle spectrometry

As a reference method to perform absolute measurements of the implanted ^{226}Ra activity, α-particle spectrometry under defined solid angle (DSA) was applied, which is among the most accurate primary methods for activity determination for α-particle emitters, achieving standard uncertainties routinely below 1% (Arinc et al., 2016; Pommé, 2015). This technique was carried out utilizing the PTB DSA α-particle spectrometer M10 with an approximate geometrical efficiency of 1% of 4π sr. The basis of this method is the exact determination of the solid angle of the radiation source subtended by the detector, which is in practice realized by an aperture system opaque to α-particles. The knowledge of the aperture geometry allows calculating the detection efficiency employing Monte-Carlo integration of (2), i.e., through path tracing of randomly generated rays within the source area A. The geometrical efficiency G is given by

$$G = \frac{1}{4\pi} \frac{\int_A \Omega_{\mathrm{d}A} w_{\mathrm{d}A} \mathrm{d}A}{\int_A w_{\mathrm{d}A} \mathrm{d}A} \tag{2}$$

where A denotes the total area of the radiation source, dA an area element within A, $\Omega_{\mathrm{d}A}$ the solid angle subtended by the detector with respect to dA and $w_{\mathrm{d}A}$ the relative contribution of activity contained within dA to the total activity.

The geometrical parameters of the setup are known precisely and traceably to PTB standards and result in an accuracy of 0.25% in the calculated geometrical efficiency. They are given in more detail in (Mertes et al., 2020). The dead time of the system is corrected for by a high-precision pulse generator, which is connected to the system pre-amplifier operating at a nominal repetition rate of 50 Hz with negligible uncertainty. The employed ion-implanted, passivated Si-diode detector in the *M10* setup is a Canberra PIPS® of 600 mm^2 active area and 300 µm depletion depth with a rated energy resolution (FWHM) of 20 keV at 5.5 MeV. Fig. 4 shows typical α-particle spectra of the produced Al- and W-targets, which were implanted with ^{226}Ra as given above. The spectra were obtained approximately 2 months after implantation and show a slight variation in energy resolution between the different target materials. Nevertheless, overall unmatched energy resolution is observed if compared with the 20 keV FWHM reported in (Marouli et al., 2017) and specifically in (Mertes et al., 2020), measured with the same setup for electrodeposited ^{226}Ra. In Fig. 4, the two spectra with the highest deviation in resolution are deliberately accentuated. The average observed FWHM of the higher energy ^{226}Ra peaks amount to 16.8 keV (W) and 15.6 keV (Al) respectively, obtained from a graphical method.

In order to determine the exact measurement geometry, a digital autoradiograph of each source was taken with a FUJIFILM FLA-9000, which yields intensity values on a 100 × 100 grid of (0.2 × 0.2) mm^2 pixels. As an example, Fig. 5 shows a radiograph obtained in this way. The targets are centered with respect to the grid by using four ^{238}Pu reference point sources placed rectangularly around the target. All resulting autoradiographs show bivariate Gaussian distributions with a variance of approximately 1 mm in both directions, i.e., a FWHM of about 2.3 mm. The obtained data is interpreted as the projected activity distribution. Thus, in the Monte-Carlo integration of (2), the autoradiography data is employed directly for the sampling of origin points of random paths to be tracked, where uniform distributions within each pixel are assumed for oversampling.

Due to the non-central installation of targets in the Faraday Cup during implantation, each radiograph shows slightly different eccentricity. Therefore, the computation of the geometrical efficiency G was carried out for each source independently. All geometrical parameters were iteratively resampled to obtain a population of G around its mean value, as similarly reported in (Arinc et al., 2016), including the

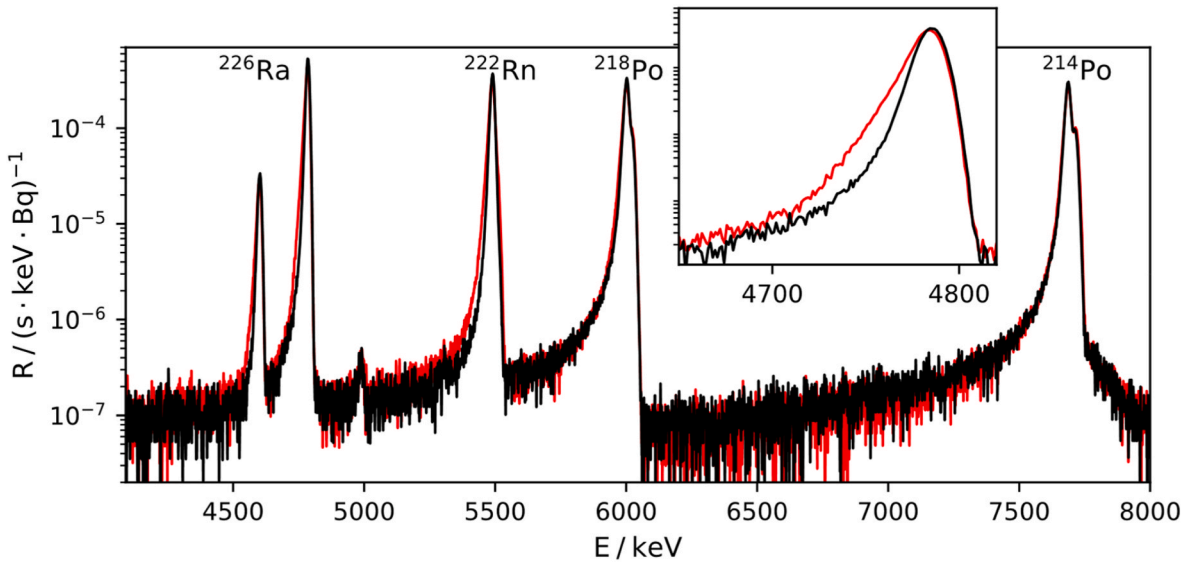

Fig. 4. Depiction of collected α-particle spectra for targets 2018-1122 (W target, red) and 2018-1133 (Al target, black), normalized to activity and measurement time with a magnified view of the higher energy ^{226}Ra emission. (For interpretation of the references to color in this figure legend, the reader is referred to the Web version of this article.)

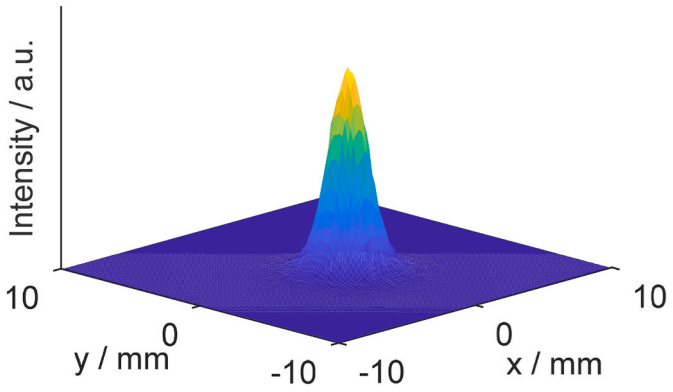

Fig. 5. Depiction of a typical digital autoradiograph of implanted ^{226}Ra activity of target 2018-1121 (W) as an example. The origin coincides with the center of the circular target.

propagation of the geometrical uncertainties in accordance with GUM supplement 1 (Joint Committee for Guides in Metrology, 2008). Since there is no control over rotations of the source between taking the radiograph and installation of the source in the spectrometer, a random rotational angle uniform in $[-\pi, \pi]$ with respect to the center of the target, as well as a Gaussian pixel-size uncertainty of 10% and a Gaussian random x,y-offset of ±0.2 mm, were included in the analysis of G.

It should be noted that the autoradiography measures the convolution of an unknown point-spread function with the true projected activity distribution, due to the finite distance between the autoradiography film and the source surface. To account for the additional uncertainty from this effect, G was also computed for the best-case activity distribution of a bivariate Gaussian with a FWHM of 0.5 mm due to the estimated beam profile from (Kieck et al., 2019b). This approach delivered a maximum deviation of 0.3% of the resulting counting efficiency from the value obtained using the autoradiography data, and hence a rectangularly distributed correction factor within [1.000,1.003] is included in the uncertainty analysis. Moreover, backscattering and self-absorption contributions to the uncertainty are estimated to be on the order of 0.2% (Mertes et al., 2020; Pommé, 2015).

Peak areas in the α-particle spectra were determined using a regression model based on the sum of exponentially modified, left-handed Gaussians, as introduced in (Bortels and Collaers, 1987) and further refined in (Pommé and Caro Marroyo, 2015). Three left-handed exponential terms were used in each α-particle peak and it was required that the ^{226}Ra 4684 keV and the 4870 keV emission share the same shape parameters. For the peaks of ^{222}Rn and the short-lived progeny, a single Gaussian was added to the peak shape model to account for the high-energy satellite peaks (see Fig. 4). The computer program *Fityk* (Wojdyr, 2010) was used to regress this model onto the observed spectra by minimizing the weighted sum of squared residuals.

From the analysis of the adjacent regions to the peak, it was estimated that the remaining uncertainty for unresolved or incorrectly modeled tailing contributions to the ^{226}Ra count rate, further denoted as R_{Ra}, corresponds to a standard uncertainty of 0.2%.

A detailed uncertainty budget listing the relative standard uncertainties and their relative contributions to the combined uncertainty for the activity determination of source 2018-1121 is given in Table 2 as an example.

1.4. Emanation theory and associated measurements

The emanation of ^{222}Rn from the implanted sources is described by the emanation coefficient, χ, which is given by the percentage of exhaled versus retained ^{222}Rn activity after the initial ^{226}Ra decay. This ratio is, in this case, largely due to recoiling and thus depends on the target material, the implantation depth, and environmental parameters. After the α-decay of ^{226}Ra, the emerging ^{222}Rn nuclei experience an average

Table 2
Uncertainty budget for DSA α-particle spectrometric activity determination of target 2018-1121, where the relative standard uncertainty of the respective components and their relative contributions to the combined uncertainty σ_A of the ^{226}Ra activity are given.

Source for uncertainty	σ / %	rel. contribution
Counting statistics	0.04	1%
Peak shape	0.20	27%
Solid angle	0.25	40%
Activity distribution	0.09	5%
Self-absorption and backscattering	0.20	27%
σ_A / %	0.4	

kinetic energy of 86 keV. Since the implantation was carried out at just 30 keV, a certain fraction of ^{222}Rn nuclei is consequently and unavoidably ejected from the source body due to their recoil energy. From theoretical considerations this recoiling fraction is mainly related to the energy dependence of the stopping power of the target material, i.e., the difference in range of 30 keV ^{226}Ra and 86 keV ^{222}Rn nuclides, keeping in mind that the recoil is isotropic, while the implantation is approximately perpendicular to the target surface. To investigate the material dependency, the two very different target materials Al and W were used for comparison. While the absolute value of the stopping power (or equivalently implantation depth) initially only has a small effect, since it applies to both the implantation as well as the recoiling process, the impact of secondary effects, such as target material sputtering on the emanation coefficient, is strongly dependent on the material and the absolute implantation depth. A prior baseline value of 0.23 was estimated for the recoil emanation coefficient for both target materials using the projected range calculation from the *Stopping and Range of Ions in Matter* (SRIM) software (Ziegler et al., 2010). This calculation gives a mean projected range of 19 nm and 5 nm for 30 keV ^{226}Ra in Al and W, respectively. Nuclei that are not ejected directly from recoiling can subsequently diffuse out of the material, depending on the respective diffusion coefficients, which are unknown. Emanation through recoil is expected to lead to much more stable emanation behavior concerning changes in environmental parameters compared to source setups, which are largely based on diffusive emanation, such as the ones discussed by (Linzmaier and Röttger, 2013) among others. This is ascribed to the fact that diffusion is strongly impacted by temperature, partial pressure gradients, and ad- and absorption of humidity, while these parameters are thought to not affect recoiling as much.

For determination of the emanation coefficient χ via the amount of permanently emanating and steadily regenerated ^{222}Rn from the sources, two types of independent, absolute measurement methods were applied. After the sources reached a steady-state (approx. after 20 days), χ is given by

$$\chi = 1 - \frac{A_{Rn}}{A_{Ra}} \tag{3}$$

where A_{Rn} and A_{Ra} denote the activity of the respective nuclide in the emanation source. Firstly, the method presented in (Linzmaier and Röttger, 2013) and (Mertes et al., 2020) was considered, which is based on the equilibrium of the γ-emitting short-lived ^{222}Rn progeny ^{214}Pb and ^{214}Bi against ^{226}Ra in the source, which is distorted due to emanation of ^{222}Rn. Secondly, the emanation coefficient was also measured by a previously unreported method derived from first principles through assessing the α-particle spectra obtained for the residual ^{222}Rn within the source. Both methods have their own drawbacks and associated sources for systematic uncertainties and biases, which are discussed in the following sections.

1.5. γ-ray spectrometric determination of the emanation coefficient

The γ-ray spectrometric method as reported in (Linzmaier and Röttger, 2013; Mertes et al., 2020) was used for γ-ray spectrometric determination of the emanation coefficients. For this method, a reference source of similar type and geometry is needed, in which the natural secular equilibrium between the short-lived ^{222}Rn progeny and ^{226}Ra is fully established through sealing against ^{222}Rn emanation. In order to obtain such reference sources, one of the sources of each target material (W, Al) was closed hermetically against ^{222}Rn emanation by gluing a stainless-steel sheet (nominal 0.05 mm thickness) onto the respective target using a 2-component epoxy resin (Delo-Duopox 01 rapid). The quality of the seal was investigated for each source produced in this way in a nominal 50 L noble-gas tight volume, in which an AlphaGuard (Saphymo, Model PQ2000) measures the ^{222}Rn-concentration. Since there was no detectable increase in ^{222}Rn concentration after flushing with aged air, the sealing was estimated to be tight to better than 0.5% loss of emanating ^{222}Rn. Conversely, previous attempts using a cyanacrylate glue yielded an unsatisfactory seal and as a result one of the sources (2018-1122) was thus cleaned from residual glue with a cotton cloth moistened in acetone. This procedure showed to remove less than 5% of the activity as investigated by subsequent α-particle spectrometry, which indicates a relatively high chemical and mechanical stability of the implanted sources.

For the determination of the emanation coefficient using γ-ray spectrometry, closely following the procedure in (Linzmaier and Röttger, 2013; Mertes et al., 2020), the full energy peak count rate ratios of the short-lived ^{222}Rn progeny ^{214}Pb and ^{226}Ra were compared with those measured for the respective sealed source. Table 4 shows results obtained by averaging data over all collected spectra and all investigated γ-ray emissions (^{214}Pb 242 keV, 295 keV, 352 keV). Since a ratio of count rates is evaluated, the effects of possible changes in geometry and differences in γ-ray attenuation between the sealed and open sources are particularly small. Slight changes in measurement geometry between the sealed and open sources resulting from potential target thickness variation on the order of 0.1 mm are assumed to introduce an uncertainty of 0.1%. Especially in the case of the W targets, measurements were only possible through the layer of epoxy-resin (as opposed to through the target material) due to the specifically high γ-ray attenuation in W. Thereby, an additional uncertainty arises from the attenuation of γ-rays within the layer of epoxy resin and stainless steel, which was analytically estimated from the Lambert-Beer law and the mass attenuation coefficients from XCOM (Berger et al., 2019) for each investigated γ-ray emission and was found to not exceed a deviation of 0.3% with respect to the count rate ratios. Due to the absolute magnitude of the emanation coefficients, relative uncertainty estimates for the count rate ratios are propagated amplified by a factor of approximately 3. An uncertainty budget for a γ-ray spectrometric determination of the emanation coefficient using the 352 keV ^{214}Pb emission for source 2018-1120 is given in Table 3 as an example.

The γ-ray spectrometric method has the drawback that it does not directly measure the ^{222}Rn within the source but progeny of ^{218}Po. Since it was assumed that the emanation of ^{222}Rn is primarily due to recoil and much less to only the diffusion of atoms, this method is potentially impacted by further recoil losses of ^{218}Po and ^{214}Pb. In addition, the necessity of the sealed reference source introduces systematic uncertainties due to potential imperfect sealing and unavoidable changes in measurement geometry. As the magnitude of these effects is partially unknown, the second method was applied to verify the results.

1.6. Absolute α-particle spectrometric determination of the emanation coefficient

The second method directly measures the α-decay of ^{222}Rn that is retained within the source. Nevertheless, it is difficult to dissect contributions of recoiling ^{222}Rn atoms that are implanted into the detector and its surroundings during α-particle spectrometric measurements, causing possible bias. The occurrence of these recoil contributions to the peaks of ^{222}Rn, ^{218}Po, and ^{214}Po in α-particle spectra was previously

Table 3
Typical uncertainty budget for the γ-ray spectrometric determination of the emanation coefficient (example for target 2018-1120 and the 352 keV ^{214}Pb emission), where the relative standard uncertainty of the respective components and their relative contributions to the propagated combined uncertainty σ_χ of χ are given.

Source for uncertainty	σ / %	rel. contribution
Counting statistics	0.3	40%
Change in geometry	0.1	5%
γ-ray attenuation	0.17	15%
Incomplete sealing	0.29	40%
σ_χ / %	1.1	

Table 4
Comparison of determined emanation coefficients of the implanted ^{226}Ra sources using α-particle spectrometry (χ_α) and γ-ray spectrometry (χ_γ) and observed FWHM in α-particle spectra of the 4784 keV *^{226}Ra emission.*

Target (Material)	χ_α	χ_γ	FWHM ^{226}Ra/keV
2018-1120(W)	0.308 (4)	0.3077 (29)	16.5
2018-1121(W)	0.340 (4)	0.341 (5)	16.8
2018-1122(W)	0.285 (4)	-	17.1
2018-1133(Al)	0.273 (4)	0.272 (4)	15.3
2018-1134(Al)	0.260 (3)	-	15.5
2018-1128(Al)	0.233 (4)	0.230 (4)	16.0

reported for electrodeposited ^{226}Ra sources in (Marouli et al., 2017), while in (Jurado Vargas et al., 1995) measurements of the emanation using α-particle spectrometry were reported, which seemingly neglected this fact. Moreover, α-particle spectra are recorded under low to medium vacuum conditions of typically few 10^{-1} Pa, which might affect the derivation of the emanation coefficient both by changing the chemical composition in the source material through drying and desorption and by the resulting pressure gradients.

As pointed out, for the determination of the emanation coefficient from the obtained α-particle spectra, the ingrowing secondary background generated by ^{222}Rn atoms recoiling into the detector must be corrected, especially in case of prolonged measurements. For illustration, Fig. 6 depicts the observed evolution of the ^{222}Rn-peak of an α-particle spectrum over time.

The approach of peak deconvolution commonly applied in α-particle spectrometry was experienced to be unreliable and unsatisfactory for the deconvolution of the strongly overlapping ^{222}Rn and recoil ^{222}Rn peaks without using temporal information.

This is due to the high degrees of freedom of the available various peak-shape models, reported in (Pommé and Caro Marroyo, 2015) among others, which lead to numerical instability, overfitting, and high sensitivity to starting parameters. Moreover, the distribution of plausible parameters is thought to be strongly correlated and multi-modal since different combinations of tailing parameters of the two contributing peaks can lead to indistinguishable likelihoods, essentially attributing either too much or too little of the peak area to the respective secondary background or source contributions, arising from the overlapping left-handed tailings. Possible strategies to resolve this are either to incorporate shape information on the secondary background peak or to use time-domain information and ingrowth modeling. Shape information could be acquired by subsequent measurements but several complications were experienced using this strategy. These arise from the

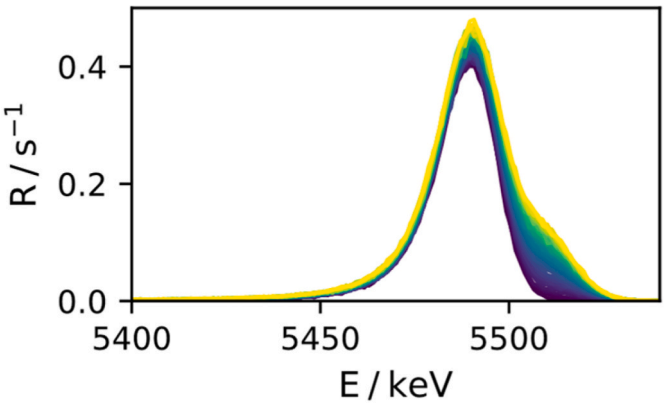

Fig. 6. Typical ingrowth of the observed α-particle peak of ^{222}Rn. Time development since installation of the source is given by color-coding from blue (start) to yellow (end) throughout approx. 7 d. The ingrowing satellite peak is due to ^{222}Rn recoil implantation into the detector. (For interpretation of the references to color in this figure legend, the reader is referred to the Web version of this article.)

limited statistics collectible during the decay and gain drifts that distort the spectra. The computation of meaningful uncertainty estimates in this case requires computationally intensive Monte-Carlo sampling, which was found to be impracticable. Therefore, in this work, the choice was made to use time-domain information to dissect the secondary background contributions to the combined peak. In order to make progress in modeling the ingrowth of the recoiled ^{222}Rn to the overall counting rate in the combined ^{222}Rn peak, a simple method was derived, as described below. As previously stated, the area of the combined peak was determined by regression of the sum of a triple-tailed, exponentially modified Gaussian and a single Gaussian for the satellite peak, intentionally not attempting to deconvolve the relative contributions but to determine the combined peak area.

The counting rate in the combined ^{222}Rn peak is assumed to be the sum of the differently weighted, time-integrated activities in the source and the detector, respectively.

$$R'(t,r) = \frac{\varepsilon_{Rn}}{r}\int_{t}^{t+r} A_{Rn}(\tau)\mathrm{d}\tau + \frac{\varepsilon_i}{r}\int_{t}^{t+r} A_i(\tau)\mathrm{d}\tau \tag{4}$$

where $R'(t,r)$ is the apparent, combined count rate of the ^{222}Rn peak at time instant t, observed in a spectrum obtained over the real-time interval r. A_{Rn} and A_i denote the ^{222}Rn activity in the source and the recoil implanted activity in the detector and surroundings, respectively, which are measured with counting efficiencies ε_{Rn} and ε_i.

For A_{Rn} and A_i, the following first-order continuity equations are formulated, assuming that the emanation coefficient is constant and that the source already reached the associated equilibrium state.

$$\frac{\mathrm{d}A_{Rn}}{\mathrm{d}t} = 0 \quad \frac{\mathrm{d}A_i}{\mathrm{d}t} = -\lambda_{Rn}A_i + k \tag{5}$$

where λ_{Rn} denotes the decay constant of ^{222}Rn and k denotes a latent ingrowth term in activity per unit time.

By substituting the solutions of the continuity equations and carrying out the integration, equation (6) was derived for the observed combined count rate corrected for recoil contributions present at the start of the measurements due to remaining recoiled ^{222}Rn from previous measurements, resulting in the count rate $R_{i,0}$. $R_{i,0}$ was determined by extrapolation from previous background measurements through weighted linear least squares.

$$R'(t,r) - R_{i,0}f = R_{Rn} + \frac{R_{i,0}}{r}f + R_{i,\infty}(1-f) \tag{6}$$

where $f(t,r) = \frac{e^{-\lambda_{Rn}t}}{r\lambda_{Rn}}(1 - e^{-\lambda_{Rn}r})$, $R'(t,r)$ is the apparent combined count rate at measurement start time t with the associated real-time interval r, $R_{i,0}$ is the count rate generated by the recoil implanted ^{222}Rn at the beginning of the installation of a source, $R_{i,\infty}$ is the associated equilibrium value, and R_{Rn} is the count rate due to the ^{222}Rn activity of the source. Equation (6) can be seen as a linear regression with respect to the parameters and the independent variable $1 - f(t,r)$ for pairs of t and r, which was carried out by weighted linear least squares through numerical matrix inversion. The covariance structure on the dependent variable, $R' - R_{i,0}f$, resulting from uncertain $R_{i,0}$, was taken into account by first computing its covariance matrix made up of the counting statistics and the contributions due to $R_{i,0}$ and using its inverse as the weights. This allows for direct propagation of the uncertainty associated with $R_{i,0}$. The uncertainty arising from λ_{Rn} (0.02%) was disregarded in this analysis as it was considered negligible. A typical result of this procedure is shown in Fig. 7.

The absence of ^{210}Po due to the mass-separation process was found to allow for a more precise determination of the ^{222}Rn peak area. Otherwise a slight overlap between the ^{222}Rn (5489 keV) tailing and the ^{210}Po peak (5304 keV) would have disturbed the data. For this analysis the dead-time of the system was neglected since only the ratio of count rates

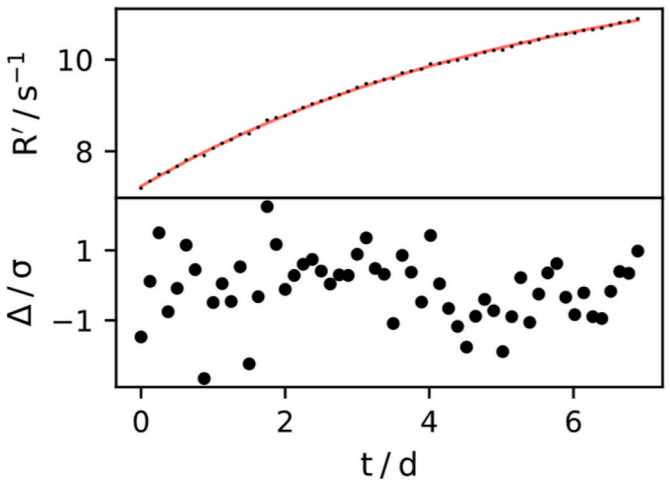

Fig. 7. Modeled ingrowth behavior of combined ^{222}Rn α-particle peak count rate (top) of source 2018-1121 and associated normalized residuals (bottom).

is needed, which is unaffected by the dead-time.

This procedure was carried out for each of the 6 produced sources and the respective emanation coefficients were calculated, extending (3) by the regression parameter R_{Rn} and the average count rate of the ^{226}Ra peak R_{Ra}, as was already evaluated previously for the ^{226}Ra activity measurements.

$$\chi = 1 - \frac{A_{Rn}}{A_{Ra}} = 1 - \frac{R_{Rn}}{R_{Ra}} \tag{7}$$

The main contribution to the combined uncertainty is due to the potential systematic anti-correlation of R_{Rn} and R_{Ra} caused by imperfect determination of contributions of the tail of the ^{222}Rn peak to the ^{226}Ra peak. Since the uncertainty of R_{Ra} is 0.2% due to remaining tailing contributions, a worst-case of 0.4% is estimated for the uncertainty of the activity ratios due to this anti-correlation, assuming pessimistically that all unresolved contributions to R_{Ra} belonged to R_{Rn}. Due to the emanation coefficients on the order of 0.3, this results in a worst-case systematic uncertainty of about 1% in the emanation coefficients, which is reflected in the uncertainty given in Table 4, where the resulting emanation coefficients from both analyses are tabulated. Very good agreement between both approaches to better than 1% was shown, indicating their equivalence and accuracy. Similarly, both methods turned out to lead to comparable uncertainty, largely caused by the estimation of systematic contributions.

1.7. Stability of emanation coefficients with respect to environmental conditions

For a full characterization of the emanation sources, measurements of one of them (Al, 2018-1133) were carried out in a 20 m^3 climate chamber at varying relative humidity in the range of 15 %rH to 70 %rH at 21 °C–32 °C using an electrically cooled HPGe detector and a 1.5" $LaBr_3$ detector with the implanted target mounted in the middle of both detectors. To fit both detectors, a partially open lead shield as shown in Fig. 8 was used. Detectors were operated with acquisition times of 12 h. Temperature and relative humidity were recorded in proximity to the implanted target with a SHT-35 sensor.

Fig. 9 shows the evolution of the normalized count rate ratio of the full-energy peaks of the 352 keV ^{214}Pb and 186 keV ^{226}Ra emissions to a steep change in humidity from 15 %rH to 70 %rH. No significant (two-sided, unequal variance T-test, $p = 0.60$) deviation could be found in the mean values before and after the change. The detection limit was estimated by calculating the critical value of change, for which this statistical test would yield $p < 0.05$, which corresponds to a change in the emanation of approximately 1% at a 95% significance level.

Fig. 10 shows the change of this count rate ratio for a temperature increase from 21 °C to 32 °C. It was found that within the time and the uncertainty of the measurements, the mean value of the ratio decreased by 0.8% in conjunction with increasing temperature, which is significant ($p < 0.002$). This change corresponds to an increase in the emanation of approximately 2%. Gain drifts with respect to temperature were corrected by calculating a distinct energy calibration for each spectrum, however, drift within the integration time could not be corrected, which potentially contributes to the observed deviation due to inaccuracies in peak area determination, especially in the case of the strongly temperature-dependent $LaBr_3$ detector. Changes in the counting efficiency due to temperature expansion were not corrected, since they were considered negligible in this temperature range. The observed decrease in the count rate ratio is likely caused by the source itself

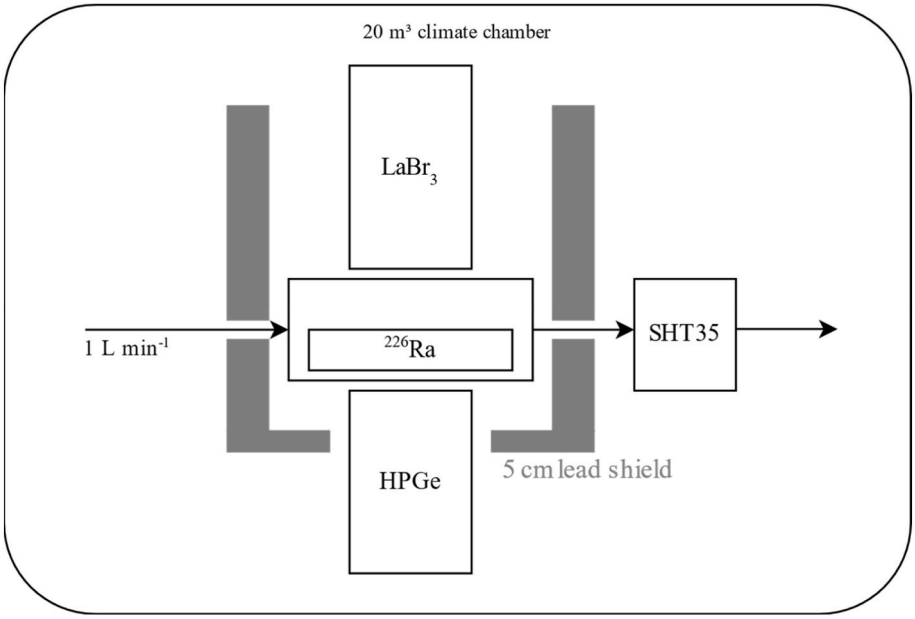

Fig. 8. Schematic of the γ-ray spectrometry setup in a 20 m^3 climate chamber used in this work.

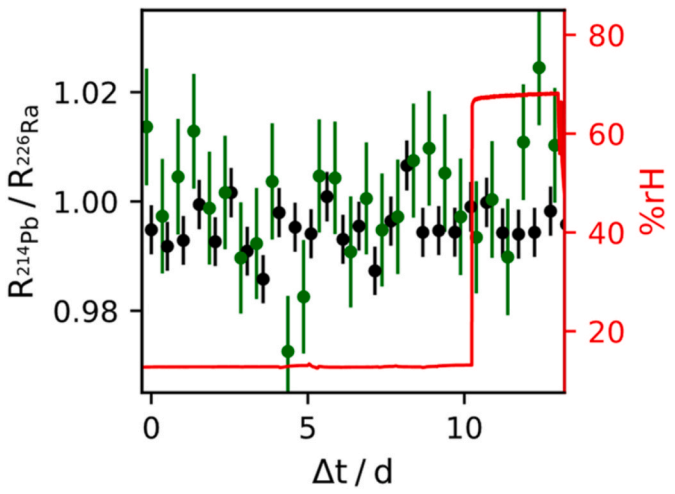

Fig. 9. Normalized count rate ratios of the 352 keV ^{214}Pb and 186 keV ^{226}Ra emission measured with a 1.5″ $LaBr_3$ (green) detector and a HPGe (black) detector at varying relative humidity from 15 %rH to 70 %rH (red). (For interpretation of the references to color in this figure legend, the reader is referred to the Web version of this article.)

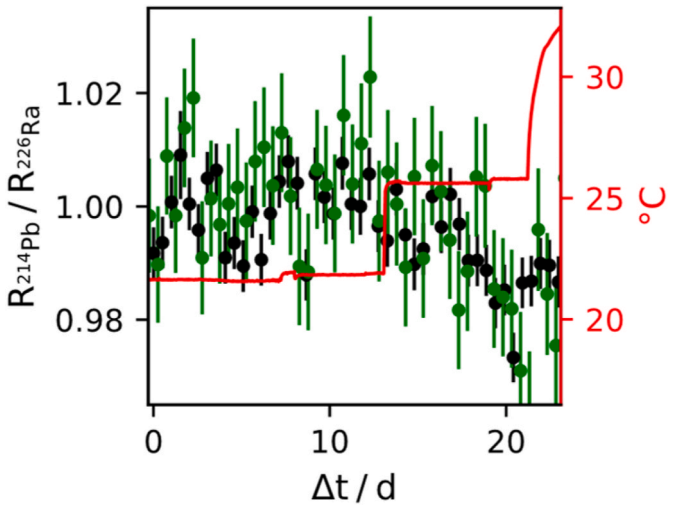

Fig. 10. Normalized count rate ratios of the 352 keV ^{214}Pb and 186 keV ^{226}Ra emission measured with a 1.5″ $LaBr_3$ (green) detector and a HPGe (black) detector at varying temperature (red). (For interpretation of the references to color in this figure legend, the reader is referred to the Web version of this article.)

because both detectors yielded comparable results, while a change of counting efficiency at different energies and gain drift is expected to have different effects on each detector.

2. Discussion and conclusions

Ion implantation of ^{226}Ra at high isobaric and isotopic purity was successfully carried out at the RISIKO laser mass separator of Mainz University to create high quality, radiometrically and chemically pure ^{222}Rn emanation sources. The comparison of α-particle spectrometry for the determination of the implantation efficiency exhibits overall good agreement with the ion current measurements, considering that an uncertainty of 10% was assumed for the ion current measurements due to sputtering effects in the detector system. This validates the ion current and implantation efficiency measurements of the mass separator facility to within this uncertainty and indicates the isotopic and isobaric purity since the method applies only when all ions are indeed $^{226}Ra^{+}$. When comparing the ion current measurements, and keeping in mind that target 2018-1120 was implanted under unfavorable conditions during initial beamline optimizations, a slight target material dependency can be hypothesized. This might be related to the different sputtering yields and charge distributions of sputtered ions related to the different target materials. Due to the negative potential of the Faraday cup repeller electrode, secondary electron emission is suppressed and the probable loss of charge from escaping positively charged sputtered ions generally leads to underestimation of the implanted activity. However, the prolonged implantation results in the sputtering of already implanted ^{226}Ra, which distorts the ion current measurements in the opposite direction, especially in the case of the shallow implantation depth of the W targets.

Nonetheless, a good implantation efficiency on the order of 50% was achieved by employing a two-step laser ionization scheme on top of surface ionization in a hot tantalum cavity. The high quality of the resulting emanation sources is highlighted by the unusually high resolution in the obtained α-particle spectra.

Moreover, it was observed that emanation coefficients in the range of 0.23–0.34 are achievable using ion implantation at 30 keV depending on the target material, which is relatively close to our rough theoretical estimate of the recoil-loss probability for ^{222}Rn from the calculation of the projected transmission ranges through SRIM. In the case of tungsten targets the deviation from the predicted recoil emanation coefficient was found to be more pronounced than for aluminum, and it was found that this deviation increased with increasing amounts of implanted ^{226}Ra. This effect is clearly related to target material sputtering having a greater effect in the case of W target due to the shallow depth profile of implanted ^{226}Ra. The sole exception of this trend is target 2018-1128, in which experimental difficulties potentially caused by a vacuum breakdown changed the structure of the target, resulting in a clearly visible amorphization of the target, unlike the other targets. During the measurements in the climate chamber, the temperature dependence of the emanation was apparent. We hypothesize from this that there is indeed a non-negligible contribution of diffusing ^{222}Rn to the overall emanation and that the higher emanation in the case of tungsten targets might thus also be explained by different diffusion properties. While it is well known that the emanation of ^{222}Rn shows a strong humidity dependence for many materials, especially porous ones, (e.g., Janik et al., 2015; Stranden et al., 1984; Zhou et al., 2020), a correlation between humidity and emanation for implanted ^{226}Ra sources, remarkably, could not be identified in this study, which is in line with our prior assumptions.

To account for possible recoil losses of short-lived progeny, which might invalidate previously reported measurement techniques, a new absolute method to determine the emanation coefficient of such sources using α-particle spectrometry was developed. Exceptionally good agreement to the previously established γ-ray spectrometric methods was found, giving strong confidence to both techniques. For statistical reasons and lower sensitivity coefficients for systematic uncertainties, higher emanation coefficients and especially their variations are easier and more accurately measurable. This in turn means that conservative estimation of systematic uncertainties leads to potentially strongly overestimated uncertainties in the emanation coefficients, indicated by the excellent agreement between both methods for its determination, whereas observed deviations were below these conservative uncertainty estimates. Moreover, the agreement between the different methods underpins the findings of high stability of the emanation coefficient with respect to humidity, since the α-particle spectra are recorded in vacuum conditions.

For the determination of the implanted activity, the DSA α-particle spectrometry method yielded relative uncertainties down to 0.4%. The emanation coefficients were determined with combined relative uncertainty on the order of 1%, with potential for improvement by prolonged measurement times and more elaborate peak deconvolution in case of the α-particle spectrometric method. A method to simultaneously regress the ingrowth of the recoil ^{222}Rn peak and the observed time

series of α-particle spectra could potentially improve the estimation of systematic uncertainty. Unfortunately, that is beyond the scope of this study due to the vast computational complexity.

The produced emanation sources can be used to establish time-stable, SI-traceable ^{222}Rn reference atmospheres at a combined uncertainty below 2% with ^{222}Rn source terms between 340 μBq s^{-1} and 820 μBq s^{-1}, even at variable humidity. A possible path for improvement, especially concerning the determination of emanation coefficients, is to change the implantation depth profile either by adjustment of the implantation energy or by mounting the target at an angle with respect to the ion beam, which is expected to increase the emanation coefficients and thus result in even higher accuracy of the presented measurement techniques.

Overall, the ion implantation process was found to be a very promising technique for the production of stable, low-level ^{222}Rn emanation standards of highest metrological quality. This was due to the high degree of control manifested in the achievable accuracy of characterization techniques, with clear paths for further improvement and without the need for standardized ^{226}Ra solutions.

Declaration of competing interest

The authors declare that they have no known competing financial interests or personal relationships that could have appeared to influence the work reported in this paper.

Acknowledgment

This project 19ENV01 traceRadon has received funding from the European Metrology Programme for Innovation and Research (EMPIR) programme co-financed by the Participating States and from the European Union's Horizon 2020 research and innovation programme.19ENV01 traceRadon denotes the EMPIR project reference.

References

Arinc, A., Parfitt, M.J., Keightley, J.D., Wilson, A., 2016. Defined solid angle alpha counting at NPL. Appl. Radiat. Isot. 109, 198–204. https://doi.org/10.1016/j.apradiso.2015.11.073.

Bé, M.-M., Chisté, V., Dulieu, C., Browne, E., Chechev, V., Kuzmenko, N., Helmer, R., Nichols, A., Schönfeld, E., Dersch, R., 2004. Table of Radionuclides, Monographie BIPM-5. Bureau International des Poids et Mesures, Pavillon de Breteuil, F-92310 Sèvres, France.

Berger, M.J., Hubbell, J.H., Seltzer, S.M., Chang, J., Coursey, J.S., Sukumar, R., Zucker, D.S., Olsen, K., 2019. XCOM: Photon Cross Section Database Version 1.5. National Institute of Standards and Technology, Gaithersburg, MD.

Bortels, G., Collaers, P., 1987. Analytical function for fitting peaks in alpha-particle spectra from Si detectors. Int. J. Radiat. Appl. Instrumentation. Part 38, 831–837. https://doi.org/10.1016/0883-2889(87)90180-8.

Day Goodacre, T., Billowes, J., Binnersley, C.L., Bissell, M.L., Chrysalidis, K., Cocolios, T. E., de Groote, R.P., Farooq-Smith, G.J., Fedorov, D.V., Fedosseev, V.N., Flanagan, K. T., Franchoo, S., Garcia Ruiz, R.F., Gins, W., Heinke, R., Koszorús, Á., Lynch, K.M., Marsh, B.A., Molkanov, P.L., Naubereit, P., Neyens, G., Ricketts, C.M., Rothe, S., Seiffert, C., Seliverstov, M.D., Stroke, H.H., Studer, D., Vernon, A.R., Wilkins, S.G., Wendt, K.D.A., Yang, X.F., 2018. Radium ionization scheme development: the first observed autoionizing states and optical pumping effects in the hot cavity environment. Spectrochim. Acta Part B At. Spectrosc. 150, 99–104. https://doi.org/10.1016/j.sab.2018.10.002.

Fedosseev, V., Chrysalidis, K., Goodacre, T.D., Marsh, B., Rothe, S., Seiffert, C., Wendt, K., 2017. Ion beam production and study of radioactive isotopes with the laser ion source at ISOLDE. J. Phys. G Nucl. Part. Phys. 44, 084006 https://doi.org/10.1088/1361-6471/aa78e0.

Janik, M., Omori, Y., Yonehara, H., 2015. Influence of humidity on radon and thoron exhalation rates from building materials. Appl. Radiat. Isot. 95, 102–107. https://doi.org/10.1016/j.apradiso.2014.10.007.

Joint Committee for Guides in Metrology, 2008. Evaluation of Measurement Data — Supplement 1 to the JCGM, vol. 101, p. 90.

Jurado Vargas, M., de Soto, F.F., Sánchez, A.M., 1995. Energy resolution, yield and radon diffusion in the electrodeposition of radium. Nucl. Instrum. Methods Phys. Res. A 364, 349–353. https://doi.org/10.1016/0168-9002(95)00393-2.

Jurado Vargas, M., Fernández De Soto, F., 1996. A study of 222Rn emanation in electrodeposited sources of 226Ra with barium. Nucl. Instruments Methods Phys. Res. Sect. A Accel. Spectrometers, Detect. Assoc. Equip. 368, 488–491. https://doi.org/10.1016/0168-9002(95)00854-3.

Kieck, T., Biebricher, S., Düllmann, C.E., Wendt, K., 2019a. Optimization of a laser ion source for 163 Ho isotope separation. Rev. Sci. Instrum. 90, 053304 https://doi.org/10.1063/1.5081094.

Kieck, T., Dorrer, H., Düllmann, C.E., Gadelshin, V., Schneider, F., Wendt, K., 2019b. Highly efficient isotope separation and ion implantation of 163Ho for the ECHo project. Nucl. Instruments Methods Phys. Res. Sect. A Accel. Spectrometers, Detect. Assoc. Equip. 945, 162602 https://doi.org/10.1016/j.nima.2019.162602.

Kramida, A., Ralachenko, Y., Reader, J., 2020. NIST atomic spectra database [WWW Document]. https://doi.org/10.18434/T4W30F.

Lassen, J., Li, R., Raeder, S., Zhao, X., Dekker, T., Heggen, H., Kunz, P., Levy, C.D.P., Mostanmand, M., Teigelhöfer, A., Ames, F., 2017. Current developments with TRIUMF's titanium-sapphire laser based resonance ionization laser ion source. Hyperfine Interact. 238, 33. https://doi.org/10.1007/s10751-017-1407-9.

Linzmaier, D., Röttger, A., 2013. Development of a low-level radon reference atmosphere. Appl. Radiat. Isot. 81, 208–211. https://doi.org/10.1016/j.apradiso.2013.03.032.

Marouli, M., Pommé, S., Van Ammel, R., García-Toraño, E., Crespo, T., Pierre, S., 2017. Direct measurement of alpha emission probabilities in the decay of 226 Ra. Appl. Radiat. Isot. 125, 196–202. https://doi.org/10.1016/j.apradiso.2017.04.029.

Mattolat, C., Rothe, S., Schwellnus, F., Gottwald, T., Raeder, S., Wendt, K., Iguchi, T., Watanabe, K., 2009. An all-solid-state high repetiton rate titanium:sapphire laser system for resonance ionization laser ion sources. In: AIP Conference Proceedings. AIP, pp. 114–119. https://doi.org/10.1063/1.3115586.

Mertes, F., Röttger, S., Röttger, A., 2020. A new primary emanation standard for Radon-222. Appl. Radiat. Isot. 156, 108928. https://doi.org/10.1016/j.apradiso.2019.108928.

Philip Horwitz, E., Chiarizia, R., Dietz, M.L., 2007. A novel strontium-selective extraction chromatographic resin. Solvent Extr. Ion Exch. 10, 313–336. https://doi.org/10.1080/07366299208918107.

Pommé, S., 2015. The uncertainty of counting at a defined solid angle. Metrologia 52, S73–S85. https://doi.org/10.1088/0026-1394/52/3/S73.

Pommé, S., Caro Marroyo, B., 2015. Improved peak shape fitting in alpha spectra. Appl. Radiat. Isot. 96, 148–153. https://doi.org/10.1016/j.apradiso.2014.11.023.

Raeder, S., Lassen, J., Heggen, H., Teigelhöfer, A., 2014. In-source spectroscopy on astatine and radium for resonant laser ionization. Hyperfine Interact. 227, 77–83. https://doi.org/10.1007/s10751-014-1040-9.

Rothe, S., Marsh, B.A., Mattolat, C., Fedosseev, V.N., Wendt, K., 2011. A complementary laser system for ISOLDE RILIS. J. Phys. Conf. Ser. 312, 052020 https://doi.org/10.1088/1742-6596/312/5/052020.

Sonnenschein, V., Moore, I.D., Pohjalainen, I., Reponen, M., Rothe, S., Wendt, K., 2015. Intracavity frequency doubling and difference frequency mixing for pulsed ns Ti: sapphire laser systems at on-line radioactive ion beam facilities. In: Proceedings of the Conference on Advances in Radioactive Isotope Science (ARIS2014). Journal of the Physical Society of Japan. https://doi.org/10.7566/JPSCP.6.030126.

Stranden, E., Kolstad, A.K., Lind, B., 1984. The influence of moisture and temperature on radon exhalation. Radiat. Protect. Dosim. 7, 55–58. https://doi.org/10.1093/oxfordjournals.rpd.a082962.

Teigelhöfer, A., Bricault, P., Chachkova, O., Gillner, M., Lassen, J., Lavoie, J.P., Li, R., Meißner, J., Neu, W., Wendt, K.D.A., 2010. Grating tuned Ti:Sa laser for in-source spectroscopy of Rydberg and autoionizing states. Hyperfine Interact. 196, 161–168. https://doi.org/10.1007/s10751-010-0171-x.

Wendt, K., Ahmad, S.A., Klempt, W., Neugart, R., Otten, E.W., Stroke, H.H., 1987. On the hyperfine structure and isotope shift of radium. Z. Physik D Atoms, Mol. Clust. 4, 227–241. https://doi.org/10.1007/BF01436633.

Wojdyr, M., 2010. Fityk : a general-purpose peak fitting program. J. Appl. Crystallogr. 43, 1126–1128. https://doi.org/10.1107/S0021889810030499.

Zhou, Q., Shubayr, N., Carmona, M., Standen, T.M., Kearfott, K.J., 2020. Experimental study of dependence on humidity and flow rate for a modified flowthrough radon source. J. Radioanal. Nucl. Chem. 324, 673–680. https://doi.org/10.1007/s10967-020-07081-0.

Ziegler, J.F., Ziegler, M.D., Biersack, J.P., 2010. Srim – the stopping and range of ions in matter (2010). Nucl. Instrum. Methods Phys. Res. Sect. B Beam Interact. Mater. Atoms 268, 1818–1823. https://doi.org/10.1016/j.nimb.2010.02.091.